Ionic conductivity of oxy-apatite $La_{10}Si_{6-x}In_xO_{27-\delta}$ solid electrolyte ceramics

CrossMark

Jun Xiang, Zhan-Guo Liu, Jia-Hu Ouyang*, Fu-Yao Yan

School of Materials Science and Engineering, Harbin Institute of Technology, 92 West Da-Zhi Street, Harbin 150001, China

HIGHLIGHTS

- $La_{10}Si_{6-x}In_xO_{27-\delta}$ is synthesized via high-temperature solid state reaction.
- $La_{10}Si_{5.8}In_{0.2}O_{26.90}$ has a total conductivity of 3.14×10^{-2} S cm^{-1} at 1073 K.
- $La_{10}Si_{5.8}In_{0.2}O_{26.90}$ has a higher conductivity than undoped $La_{10}Si_6O_{27}$.
- $La_{10}Si_{5.6}In_{0.4}O_{26.80}$ has a thermal expansion coefficient of 9.01×10^{-6} K^{-1} at 1073 K.

ARTICLE INFO

ABSTRACT

Oxy-apatite type $La_{10}Si_{6-x}In_xO_{27-\delta}$ (x = 0.1, 0.2, 0.3, 0.4, 0.5) ceramics are synthesized via the high-temperature solid state reaction method to obtain dense bulk ceramics. Crystal structure and properties of $La_{10}Si_{6-x}In_xO_{27-\delta}$ ceramics are investigated by X-ray diffraction, scanning electron microscopy, Raman spectroscopy, complex impedance analysis and thermal expansion coefficient measurement. All the compositions of $La_{10}Si_{6-x}In_xO_{27-\delta}$ ceramics doped with In^{3+} consist of a hexagonal apatite structure with a space group $P6_3/m$. The diffraction peaks of $La_{10}Si_{6-x}In_xO_{27-\delta}$ ceramics shift to the low angle side with increasing the content of In^{3+}. Lanthanum silicates doped with trivalent In^{3+} have a higher total conductivity than those without trivalent In^{3+} at the Si^{4+} site. $La_{10}Si_{5.8}In_{0.2}O_{26.90}$ ceramics has the highest total conductivity of 3.14×10^{-2} S cm^{-1} at 1073 K, which is considerably higher than that of undoped $La_{10}Si_6O_{27}$. $La_{10}Si_{5.6}In_{0.4}O_{26.80}$ has the highest thermal expansion coefficient of 9.01×10^{-6} K^{-1} at 1073 K.

© 2013 Elsevier B.V. All rights reserved.

1. Introduction

Oxy-apatite lanthanum silicates have attracted great attention due to their low operating temperature of less than 873–1073 K, low activation energy, excellent long-term stability, a wide range of materials selection and relatively low processing cost as candidates for intermediate temperature electrolytes of solid oxide fuel cells (SOFCs) [1–5]. Recently, many researchers have studied many oxy-apatite lanthanum silicates with high oxide-ionic conductivity [6–10]. Oxy-apatite silicates are different from traditional SOFC electrolytes of fluorite and perovskite structures associated with the anion-vacancy conduction mechanism, which are novel electrolytes with a conduction mechanism of interstitial oxide-ion migration [11–20].

It is well known that the lanthanum silicates have a hexagonal oxy-apatite structure with a space group $P6_3/m$ and a stack of isolated silicate tetrahedra (SiO_4). The La cations have two kinds of sites. One is situated at seven-coordinated sites named 6h and the other is situated at nine-coordinated sites named 4f. The interstitial oxide-ions in lanthanum silicates are confirmed to migrate in the conduction channels along the c-axis via a complex sinusoidal pathway, which is the reason why the conductivity parallel to the c-axis is much higher than perpendicular to this direction [21]. Nuclear magnetic resonance (NMR) and Raman spectroscopy were also employed to identify the structure of silicate units [22–24].

Doping of cations with a relatively low valence for Si site is helpful to increase the conductivity of oxy-apatite lanthanum silicates. For example, Yoshioka et al. [25] found that the conductivity of apatite-type $La_{10}Si_6O_{27}$ is enhanced by doping of Mg^{2+}. Kendrick et al. [26] reported that a significant number of oxide ions displaced into interstitial positions and significant local structural changes are the reason why the conductivity is increased by doping with Zn^{2+}. In addition, doping of trivalent cations such as Al^{3+} and Ga^{3+} for the Si^{4+} site has also a beneficial effect on conductivity [27,28]. However, the influences of valence state and doping content on structure and electrical conductivity of oxy-apatite lanthanum

---

* Corresponding author. Tel./fax: +86 451 86414291.
  E-mail address: ouyangjh@hit.edu.cn (J.-H. Ouyang).

silicates remain still unclear. Therefore, in the present work, the crystal structure and electrical conductivity of lanthanum silicates doped with different contents of trivalent In^{3+} were investigated.

2. Experimental procedures

$La_{10}Si_{6-x}In_xO_{27-\delta}$ ($x = 0.1, 0.2, 0.3, 0.4, 0.5$) electrolytes were synthesized by the high temperature solid state reaction process. La_2O_3 (Grirem Advanced Materials Co. Ltd., Beijing, China; purity $\geq 99.9\%$), SiO_2 (Huijing New Materials Ltd., Shanghai, China; purity $\geq 99.9\%$) and In_2O_3 (Guangfu Fine Chemical Research Institute, Tianjin, China; purity $\geq 99.99\%$) powders were used as starting materials. Lanthanum oxide was precalcined at 1173 K for 2 h before weighing so as to achieve dehydration and decarbonation. These oxide powders in proper stoichiometric ratio were mechanically ball-milled in analytically pure ethanol for 24 h and then heated to 1623 K for 10 h. The as-calcined powders were uniaxially compacted in a steel mold at 20 MPa, and were then cold isostatically pressed at 260 MPa for 8 min. Finally, the compacts were pressureless-sintered at 1923 K for 10 h.

The as-sintered samples were characterized using an X-ray diffractometer (XRD, Rigaku D/Max-rB, Japan) with monochromatized Cu Kα radiation, and data were accumulated from the 2θ range of $10°-70°$ with a scanning rate of $4°$ min^{-1}. Surface morphologies of sintered samples were determined by a scanning electron microscope (SEM, Quanta 200F, USA). The dense pellets were polished and thermally etched for 30 min at a temperature, which is 50 K lower than the sintering temperature. Thermally etched surfaces of the samples were coated with a thin gold film for SEM observations with a better image definition. The bulk densities of all the sintered samples were determined by the usual volume and weight measurement technique. Raman spectra were collected by a Raman microscope (LabRAM HR800, Horiba Jobin Yvon, France). The measurements were carried out with a 458 nm line of an argon ion laser at room temperature. The laser power was 20 mW and the spot diameter was 1 μm. The range of Raman shift was from 100 to 1000 cm^{-1}.

The total conductivity of $La_{10}Si_{6-x}In_xO_{27-\delta}$ ceramics was measured by the four probe method using an AC impedance/gain-phase analyzer (Solartron™ SI 1260, UK) combined with electrochemical interface (Solartron™ SI 1287, UK) in an ambient atmosphere with the AC signal strength of 50 mV. Platinum pastes were painted on both surfaces of the specimens with 8 mm in diameter and 1 mm in thickness as the electrodes, which were heated to 1273 K for 2 h in air to erase the solvent. For the measurements of the impedance plots, data were collected from 673 to 1173 K in the frequency range of 20 Hz to 20 MHz. The temperature interval was 50 K with a stabilization time of 15 min before each measurement. The results were analyzed by the Zview software.

3. Results and discussion

3.1. Ceramic microstructures

XRD patterns of $La_{10}Si_{6-x}In_xO_{27-\delta}$ ($x = 0.1, 0.2, 0.3, 0.4, 0.5$) ceramics sintered at 1923 K for 10 h are shown in Fig. 1. The main diffraction peaks with different contents of In^{3+} correspond to the standard XRD spectrum of $La_{10}(SiO_4)_6O_3$ (JCPDS No. 53-0291), which belongs to the hexagonal apatite structure with a space group $P6_3/m$. All the samples are well crystallized. The electronegativities of elements are 1.10 for La, 1.90 for Si and 1.78 for In, respectively, so the difference in electronegativities between In and Si is clearly smaller than that between In and La, which indicates that it is more preferable for the In^{3+} to substitute Si^{4+} site firstly. In addition, as the effective ionic radii of trivalent La^{3+}, In^{3+} and
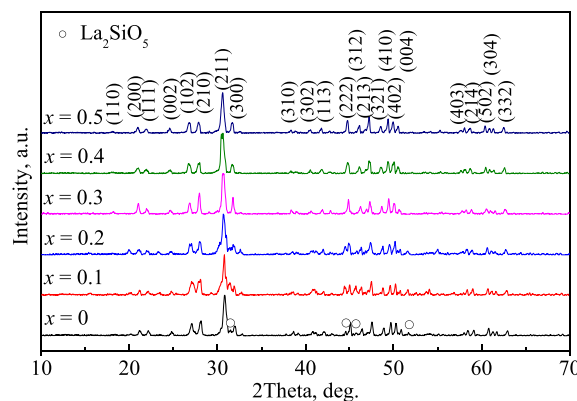

Fig. 1. XRD patterns of $La_{10}Si_{6-x}In_xO_{27-\delta}$ ceramics sintered at 1923 K for 10 h.

tetravalent Si^{4+} are $R_{La} = 0.116$ nm, $R_{In} = 0.062$ nm and $R_{Si} = 0.026$ nm, respectively, the difference in effective ionic radius between In^{3+} and Si^{4+} is also clearly smaller than that between In^{3+} and La^{3+}, which confirms that the In^{3+} cation is prior to substitute Si^{4+} site in oxy-apatite structure firstly [29]. Since the effective ionic radius of In^{3+} is larger than that of Si^{4+}, the characteristic diffraction peaks shift gradually to the low angle side with increasing the In^{3+} content, as shown in Fig. 1. However, the diffraction peaks of the second phase La_2SiO_5 reduce distinctly or even disappear, which indicates that doping with In^{3+} is beneficial to the decrease in the content of second phase La_2SiO_5. The bulk density of $La_{10}Si_{6-x}In_xO_{27-\delta}$ ceramics is determined by the usual volume and weight measurement technique, as shown in Table 1. It can be seen that the bulk density of $La_{10}Si_{6-x}In_xO_{27-\delta}$ ceramics has no distinct change with increasing the In^{3+} content. This indicates that the bulk density is not closely related to the In^{3+} content.

Fig. 2 shows the microstructures of $La_{10}Si_{6-x}In_xO_{27-\delta}$ ($x = 0.1, 0.2, 0.3, 0.4, 0.5$) ceramics sintered at 1923 K for 10 h. Obviously, $La_{10}Si_{6-x}In_xO_{27-\delta}$ ceramics have a grain size of about 10 μm, and grow uniformly and compactly. The grain boundaries are very clean, and there is no impurity at grain boundaries. The microstructures of all the samples doped with different contents of In^{3+} exhibit similar features. With increasing the content of In^{3+}, the grain size increases gradually. When the In^{3+} content is $x = 0.4$, some tiny holes appear at localized regions. When the In^{3+} content is $x = 0.5$, more tiny holes are observed on the surface of specimens, the grain boundaries become ambiguous.

3.2. Raman spectra analysis

Fig. 3 shows Raman spectra of $La_{10}Si_{6-x}In_xO_{27-\delta}$ ($x = 0.1, 0.2, 0.3, 0.4, 0.5$) ceramics sintered at 1923 K for 10 h. The band position, band relative intensity and band half-width of Raman spectra for $La_{10}Si_{6-x}In_xO_{27-\delta}$ with different In^{3+} contents are almost the same, and well correspond to undoped oxy-apatite lanthanum silicate. In this paper, major band positions of all the specimens in the range of

Table 1
Measured densities of $La_{10}Si_{6-x}In_xO_{27-\delta}$ ceramics.

Materials	Measured density, g cm^{-3}
$La_{10}Si_6O_{27}$	5.200
$La_{10}Si_{5.9}In_{0.1}O_{26.95}$	5.368
$La_{10}Si_{5.8}In_{0.2}O_{26.90}$	5.372
$La_{10}Si_{5.7}In_{0.3}O_{26.85}$	5.369
$La_{10}Si_{5.6}In_{0.4}O_{26.80}$	5.364
$La_{10}Si_{5.5}In_{0.5}O_{26.75}$	5.375

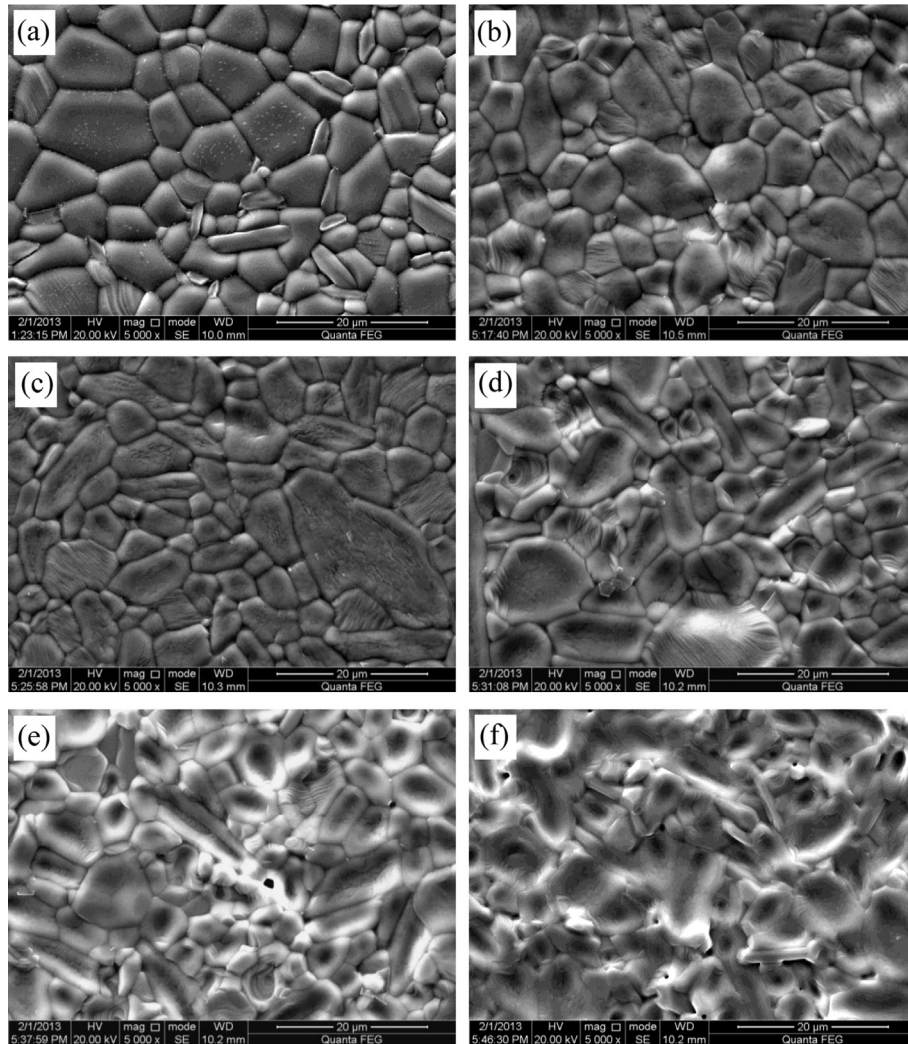**Fig. 2.** Microstructures of $La_{10}Si_{6-x}In_xO_{27-\delta}$ ceramics sintered at 1923 K for 10 h. (a) $x = 0$, (b) $x = 0.1$, (c) $x = 0.2$, (d) $x = 0.3$, (e) $x = 0.4$, (f) $x = 0.5$.

100 to 1000 cm^{-1} are approximate to those reported in previous studies related to oxy-apatites [30,31]. Two distinctly different band areas occur as divided at 350 cm^{-1} in the whole Raman range. The bands above 350 cm^{-1} are assigned to internal modes of tetrahedral SiO_4 units, while the bands below 350 cm^{-1} are
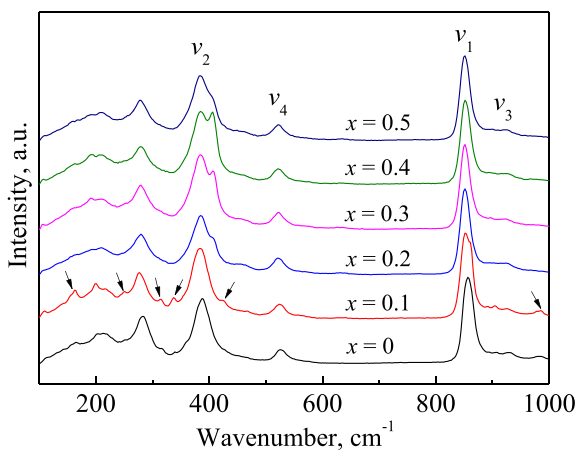

Fig. 3. Raman spectra of $La_{10}Si_{6-x}In_xO_{27-\delta}$ ceramics sintered at 1923 K for 10 h and the arrows correspond to the characteristic peaks of La_2SiO_5.

assigned to external lattice modes just as translational, vibrational and rotational of the SiO_4 units. Two main bands at 854 cm^{-1} and 385 cm^{-1} correspond to the symmetric stretching mode v_1 and the symmetric bending mode v_2 of SiO_4 tetrahedra, respectively. In addition, two weak bands at 926 cm^{-1} and 521 cm^{-1} can be assigned to the asymmetric stretching mode v_3 and the asymmetric bending mode v_4 of SiO_4 tetrahedra. All above indicate that doping with trivalent In^{3+} forms a complete solid solution, and does not bring in containing-In^{3+} impurity phase. When the doping content is $x = 0.1$, some weak bands pointed by arrows correspond to the characteristic peaks of second phase La_2SiO_5, but these characteristic peaks of second phase La_2SiO_5 disappear with further increasing the doping content. Clearly, increasing the doping content of In^{3+} could reduce or even eliminate second phase La_2SiO_5, which is in accord with the XRD results. As compared with Raman spectrum of undoped $La_{10}Si_6O_{27}$, Raman spectra of all the $La_{10}Si_{6-x}In_xO_{27-\delta}$ ($x = 0.1, 0.2, 0.3, 0.4, 0.5$) ceramics shift to the left side slightly.

3.3. Electrical conductivity

Fig. 4 shows the impedance plots at 673 K and corresponding equivalent circuit of $La_{10}Si_{6-x}In_xO_{27-\delta}$ ($x = 0.1, 0.2, 0.3, 0.4, 0.5$) ceramics. From Fig. 4, all the AC impedance spectra with different

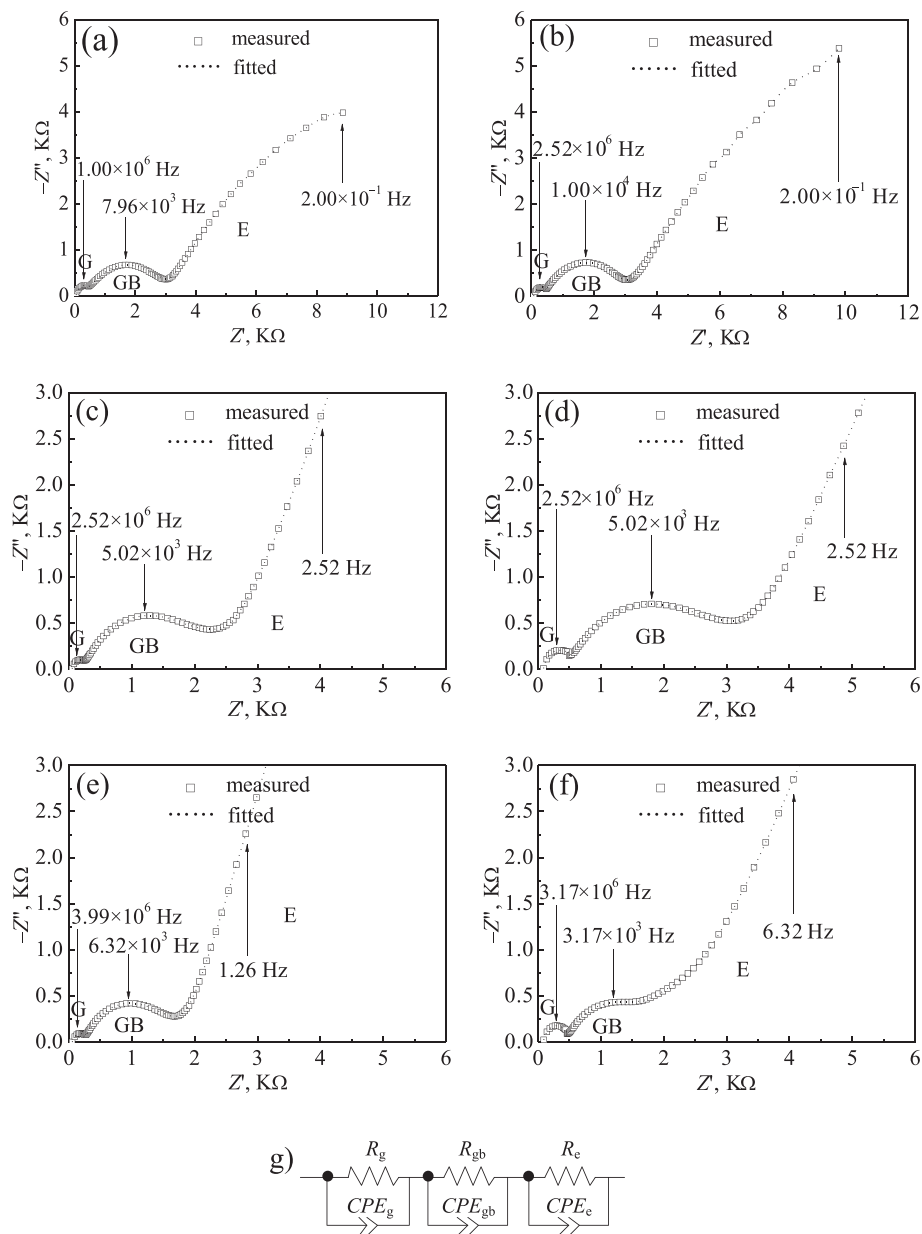**Fig. 4.** Impedance plots and corresponding equivalent circuit of La$_{10}$Si$_{6-x}$In$_x$O$_{27-\delta}$ ceramics at 673 K (a) $x = 0$, (b) $x = 0.1$, (c) $x = 0.2$, (d) $x = 0.3$, (e) $x = 0.4$, (f) $x = 0.5$, (g) equivalent circuit.

doping contents are composed of two interconnected semicircular arcs and an incomplete semicircular. Grain resistance (R_g), grain boundary resistance (R_{gb}), grain capacitance (CPE_g) and grain boundary capacitance (CPE_{gb}) for La$_{10}$Si$_{6-x}$In$_x$O$_{27-\delta}$ ceramics with different doping contents are obtained by the Zview software. The semicircular arcs at high frequency correspond to the grain impedance process and the semicircular arcs at middle frequency correspond to the grain boundary impedance process, respectively. The conduction of La$_{10}$Si$_{6-x}$In$_x$O$_{27-\delta}$ ceramics is controlled jointly by grain and grain boundary.

As compared with the AC impedance spectrum of undoped La$_{10}$Si$_6$O$_{27}$ ceramic, both the grain impedance and the grain boundary impedance of La$_{10}$Si$_{6-x}$In$_x$O$_{27-\delta}$ decrease obviously when the doping content of In^{3+} is higher than 0.1, as shown in Fig. 4. In^{3+} substitutes for Si^{4+} sites and forms a complete solid solution of La$_{10}$Si$_{6-x}$In$_x$O$_{27-\delta}$, which leads to electrostatic repulsive-force of oxide-ion sited at 2a from (InO$_4$)$^{5-}$, which is larger than from

(SiO$_4$)$^{4-}$, consequently enhances the mobility of oxide-ion, and reduces the grain impedance and grain boundary impedance. In addition, there are more oxygen vacancies generated after doping In^{3+}, which would result in large lattice distortion, and structural relaxation of La$_{10}$Si$_{6-x}$In$_x$O$_{27-\delta}$ ceramics. Thereby, the decrease in the electrostatic attraction from La^{3+} is beneficial to conduction of oxide-ions. Finally, all above-mentioned reduce the grain impedance and grain boundary impedance with increasing the In^{3+} content.

Arrhenius plots of total conductivity of La$_{10}$Si$_{6-x}$In$_x$O$_{27-\delta}$ ceramics with different contents of In^{3+} are shown in Fig. 5. Clearly, the total conductivity of La$_{10}$Si$_{6-x}$In$_x$O$_{27-\delta}$ ceramics with different doping contents is linearly related to the measurement temperature, which is well fitted to the Arrhenius equation, which demonstrates that the diffusion process of oxide-ions is thermally activated. In addition, the total conductivity of La$_{10}$Si$_{6-x}$In$_x$O$_{27-\delta}$ ceramics with different doping contents is distinctly improved as

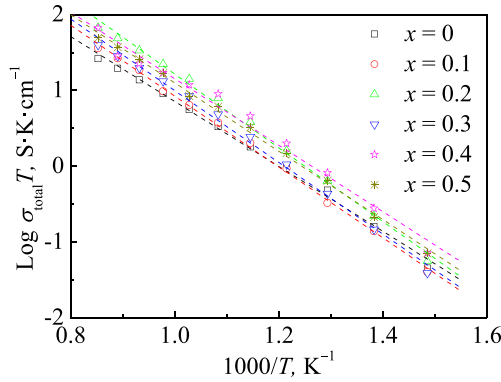**Fig. 5.** Arrhenius plots of total conductivity of $La_{10}Si_{6-x}In_xO_{27-\delta}$ ceramics.

Fig. 6. Thermal expansion curve of $La_{10}Si_{6-x}In_xO_{27-\delta}$ ceramics as a function of temperature.

compared with that of undoped $La_{10}Si_6O_{27}$ ceramics. The main carrier in undoped $La_{10}Si_6O_{27}$ ceramics is interstitial oxygen ions. However, when trivalent In^{3+} substitutes for tetravalent Si^{4+}, more oxygen vacancies will be generated in order to keep charge balance of crystal structure, and in this case the carriers contain both interstitial oxygen ions and oxygen vacancies collectively, which consequently improves the total conductivity. The activation energy E and pre-exponential factor σ_0 can be calculated from the slope and the intercept of the linear fits in the logarithmic form of the Arrhenius equation for all specimens, respectively. The activation energy E, pre-exponential factor σ_0 and the total conductivity of $La_{10}Si_{6-x}In_xO_{27-\delta}$ ceramics are shown in Table 2. At 1073 K, $La_{10}Si_{5.8}In_{0.2}O_{26.90}$ has the highest total conductivity of 3.14×10^{-2} S cm^{-1}.

3.4. Thermal expansion coefficient

Thermal expansion curve of $La_{10}Si_{6-x}In_xO_{27-\delta}$ ($x = 0.1, 0.2, 0.3, 0.4, 0.5$) ceramics as a function of temperature is shown in Fig. 6. The thermal expansion curve of all the samples with different In^{3+} contents is close to the straight line in the range of measurement temperature, and increases linearly with increasing the temperature. It demonstrates that $La_{10}Si_{6-x}In_xO_{27-\delta}$ ceramics have a good structural stability from ambient temperature to 1473 K, and no phase transition occurs during heating. However, the slope of thermal expansion curve is the largest when the In^{3+} content is $x = 0.4$. Fig. 7 presents the thermal expansion coefficients (TEC) of $La_{10}Si_{6-x}In_xO_{27-\delta}$ ceramics as a function of temperature. The TEC of $La_{10}Si_{6-x}In_xO_{27-\delta}$ ceramics increases gradually with increasing temperature, as shown in Table 3, and is distributed between 8.73×10^{-6} K^{-1} and 9.01×10^{-6} K^{-1} at 1073 K. $La_{10}Si_{5.6}In_{0.4}O_{26.80}$ has the highest TEC of 9.01×10^{-6} K^{-1} at 1073 K. The TEC of $La_{10}Si_{6-x}In_xO_{27-\delta}$ ceramics in this paper is comparable to those of traditional solid electrolytes at present and also close to those of widely-used cathode or anode materials [32,33].

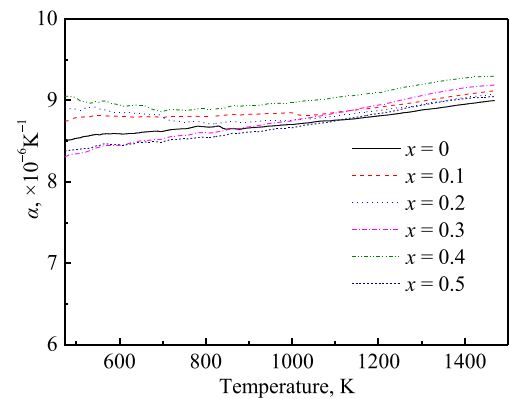**Fig. 7.** Thermal expansion coefficients of $La_{10}Si_{6-x}In_xO_{27-\delta}$ ceramics as a function of temperature.

4. Conclusions

Oxy-apatite type $La_{10}Si_{6-x}In_xO_{27-\delta}$ ($x = 0.1, 0.2, 0.3, 0.4, 0.5$) ceramics have been synthesized successfully by the high-temperature solid state reaction route. All the compositions of $La_{10}Si_{6-x}In_xO_{27-\delta}$ ceramics doped with In^{3+} consist only of a hexagonal apatite structure with a space group $P63/m$. The diffraction peaks of $La_{10}Si_{6-x}In_xO_{27-\delta}$ ceramics doped with In^{3+} shift to the low angle side with increasing the In^{3+} content. The total conductivity of all samples accords with the Arrhenius behavior. Lanthanum silicates doped with trivalent In^{3+} have a higher total conductivity than undoped $La_{10}Si_6O_{27}$. At 1073 K, $La_{10}Si_{5.8}In_{0.2}O_{26.90}$ has the highest total conductivity of 3.14×10^{-2} S cm^{-1}, which is considerably higher than that of undoped $La_{10}Si_6O_{27}$. However, $La_{10}Si_{5.6}In_{0.4}O_{26.80}$ has the highest TEC of 9.01×10^{-6} K^{-1} at 1073 K.

Table 2
Total conductivity at 1073 K and corresponding activation energy and pre-exponential factor of $La_{10}Si_{6-x}In_xO_{27-\delta}$ ceramics.

Materials	Activation energy, eV	Pre-exponential factor, S K cm^{-1}	Conductivity (1073 K), S cm^{-1}
$La_{10}Si_6O_{27}$	0.85	1.36×10^5	1.28×10^{-2}
$La_{10}Si_{5.9}In_{0.1}O_{26.95}$	0.93	3.95×10^5	1.73×10^{-2}
$La_{10}Si_{5.8}In_{0.2}O_{26.90}$	0.96	1.20×10^6	3.14×10^{-2}
$La_{10}Si_{5.7}In_{0.3}O_{26.85}$	0.94	5.29×10^5	1.84×10^{-2}
$La_{10}Si_{5.6}In_{0.4}O_{26.80}$	0.87	3.46×10^5	2.10×10^{-2}
$La_{10}Si_{5.5}In_{0.5}O_{26.75}$	0.89	3.99×10^5	2.41×10^{-2}

Table 3
Thermal expansion coefficients of $La_{10}Si_{6-x}In_xO_{27-\delta}$ ceramics at 1073 K.

Materials	α, $\times 10^{-6}$ K^{-1}
$La_{10}Si_6O_{27}$	8.75
$La_{10}Si_{5.9}In_{0.1}O_{26.95}$	8.83
$La_{10}Si_{5.8}In_{0.2}O_{26.90}$	8.79
$La_{10}Si_{5.7}In_{0.3}O_{26.85}$	8.82
$La_{10}Si_{5.6}In_{0.4}O_{26.80}$	9.01
$La_{10}Si_{5.5}In_{0.5}O_{26.75}$	8.73

Acknowledgments

References

[1] S.M. Hosseini, T. Shvareva, A. Navrotsky, Solid State Ionics 233 (2013) 62–66.
[2] M. Santos, C. Alves, F.A.C. Oliveira, T. Marcelo, J. Mascarenhas, A. Cavaleiro, B. Trindade, J. Power Sources 231 (2013) 146–152.
[3] A. Orera, T. Baikie, E. Kendrick, J.F. Shin, S. Pramana, R. Smith, T.J. White, M.L. Sanjuan, P.R. Slater, Dalton Trans. 40 (2011) 3903–3908.
[4] F. Sun, N.N. Zhang, J.L. Li, H.L. Liao, J. Power Sources 223 (2013) 36–41.
[5] S. Nakayama, A. Ikesue, Y. Higuchi, M. Sugawara, M. Sakamoto, J. Eur. Ceram. Soc. 33 (2013) 207–210.
[6] S. Nakayama, M. Sakamoto, M. Higuchi, K. Kodaira, M. Sato, S. Kakita, T. Suzuki, K. Itoh, J. Eur. Ceram. Soc. 19 (1999) 507–510.
[7] A. Mineshige, T. Nakao, M. Kobune, T. Yazawa, H. Yoshioka, Solid State Ionics 179 (2008) 1009–1012.
[8] L. Leon-Reina, J.M. Porras-Vazquez, E.R. Losilla, D.V. Sheptyakov, A. Llobet, M.A.G. Aranda, Dalton Trans. (2007) 2058–2064.
[9] J.E.H. Sansom, P.A. Sermon, P.R. Slater, Solid State Ionics 176 (2005) 1765–1768.
[10] A. Orera, P.R. Slater, Solid State Ionics 181 (2010) 110–114.
[11] M. Karlsson, Dalton Trans. 42 (2013) 317–329.
[12] V. Oygarden, T. Grande, Dalton Trans. 42 (2013) 2704–2715.
[13] Y.H. Chou, N. Hondow, C.I. Thomas, R. Mitchell, R. Brydson, R.E. Douthwaite, Dalton Trans. 41 (2013) 2472–2476.
[14] Y. Ledemi, M.E.I. Amraoui, J.L. Ferrari, P.L. Fortin, S.J.L. Ribeiro, Y. Messaddeq, J. Am. Ceram. Soc. 96 (2013) 825–832.
[15] T. Ivas, E. Povoden-Karadeniz, N. Grundy, E. Jud-Sierra, J. Grasslin, LJ. Gauckler, J. Am. Ceram. Soc. 96 (2013) 613–626.
[16] X.L. Xia, J.H. Ouyang, Z.G. Liu, J. Power Sources 189 (2009) 888–893.
[17] Z.G. Liu, J.H. Ouyang, K.N. Sun, X.L. Xia, J. Power Sources 195 (2010) 7225–7229.
[18] X.L. Xia, J.H. Ouyang, Z.G. Liu, J. Am. Ceram. Soc. 93 (2010) 1074–1080.
[19] L.P. Li, J.C. Nino, J. Eur. Ceram. Soc. 32 (2012) 3543–3550.
[20] V. Sariboga, H. Ozdemir, M.A.F. Oksuzomer, J. Eur. Ceram. Soc. 33 (2013) 1435–1446.
[21] R.F. Wu, W. Pan, X.R. Ren, C.L. Wan, Z.X. Qu, A.B. Du, Acta Mater. 60 (2012) 5536–5544.
[22] J.R. Tolchard, M.S. Islam, P.R. Slater, J. Mater. Chem. 13 (2003) 1956–1961.
[23] J.E.H. Sansom, J.R. Tolchard, D. Apperley, M.S. Islam, P.R. Slater, J. Mater. Chem. 16 (2006) 1410–1413.
[24] E. Kendrick, M.S. Islam, P.R. Slater, J. Mater. Chem. 17 (2007) 3104–3111.
[25] H. Yoshioka, S. Tanase, Solid State Ionics 176 (2005) 2395–2398.
[26] E. Kendrick, M.S. Islam, P.R. Slater, Solid State Ionics 177 (2007) 3411–3416.
[27] S. Chefi, A. Madani, H. Boussetta, C. Roux, A. Hammou, J. Power Sources 177 (2008) 464–469.
[28] E. Kendrick, P.R. Slater, Mater. Res. Bull. 43 (2008) 3627–3632.
[29] G.S. Rohrer, Cambridge University Press, Cambridge, 2004, p. 429–434.
[30] L. Zhang, Q.H. Hong, H.W. Wu, C.Z. Li, S.P. Jiang, Int. J. Hydrogen Energy 36 (2011) 6862–6874.
[31] G. Lucazeau, N. Sergent, T. Pagnier, A. Shaula, V. Kharton, F.M.B. Marques, J. Raman Spectrosc. 38 (2007) 21–33.
[32] S.A. Tabei, A. Sheidaei, M. Baniassadi, F. Pourboghrat, H. Garmestani, J. Power Sources 235 (2013) 74–80.
[33] E. Drozdz-Ciesla, J. Wyrwa, W. Pyda, M. Rekas, J. Mater. Sci. 47 (2012) 2807–2817.